Study of Rupture Directivity in a Foam Rubber Physical Model

Rasool Anooshehpoor and James N. Brune
Seismological Laboratory
University of Nevada, Reno

ABSTRACT

Foam rubber earthquake experiments provide a means to constrain parameters that control rupture dynamics (including slip evolution on the fault plane), and near-fault ground motions, offering insights that would be difficult to achieve from the limited recordings available in the near-fault region of large earthquakes.

Data from experiments simulating unilateral strike-slip motion agreed well with 3D numerical simulations of the shape, duration, and absolute amplitude of the direct acceleration pulses. Directivity was evident in both peak accelerations and pseudo-spectral accelerations, the amplitude of the fault-normal component of acceleration generally larger than the associated fault-parallel component. Waveforms agree with an empirical directivity model for earthquake strong-motion spectra at long periods.

We also investigated the effects of shallow weak layer on the near-fault ground motions. To do this we introduced plastic strips ranging in width from 4 to 20 cm (fault width =182 cm) on the fault plane. Accelerations recorded on or close to the weak layer show significant reduction in amplitudes, even though the total slip is similar to the case without a weak layer (increased slip rise-time). Surface acceleration amplitudes decrease rapidly with increasing depth of the weak layer. We also recorded results from a variety of anti-asperity (weak patch) models.

ACKNOWLEDGMENTS

CONTENTS

LIST OF FIGURES

LIST OF TABLES

INTRODUCTION

The main objective of this project is to use foam rubber modeling experiments to provide constraints on parameters that control rupture dynamics, especially forward directivity effects. Different parameterizations used in the existing numerical models lead to substantially different predictions of ground motion. Foam rubber scale models of earthquake (Brune *et al.*, 1993) provide a means for better understanding of the physical parameters that control near-field ground motions during earthquakes.

Physical models of faulting are guaranteed to obey static and dynamic mechanical laws and thus can be used to gain insight into possible physical processes involved. Of course, there are inherent problems of scaling laboratory models to the real earth. Such models can nonetheless provide important insight and constraints on numerical and theoretical models. Foam rubber models have been used in a number of studies as analogs of earthquake ruptures. Foam rubber is very flexible, *i.e.*, it has a low rigidity, making it easy to produce large strains and particle motions. Since foam rubber is light, relatively large models can be constructed, enabling the scale of dynamic phenomena to be enlarged. This allows dynamic features to be more easily observed and recorded using relatively simple electronic devices. Foam-rubber models automatically assure that motions are physically realistic (no singularities or unreasonably specified slips).

DESCRIPTION OF MODEL

The strike-slip model consists of two large blocks of foam rubber, one driven horizontally past another by a hydraulic piston. The lower block is glued to a sheet of plywood that is in turn bolted to the concrete floor (Fig. 1). The upper block and the attached rigid box are supported by four steel pipes equipped with scaffolding jacks. Normal force at the contact (fault) is provided by some fraction of the weight of the upper block (~3000 N) and is varied by lowering or raising the jacks. Shear force is provided by a hydraulic piston, which is placed between a concrete wall and the upper block's frame. As the upper block is forced to slide over the lower block, the strain in the blocks increases until the stress at the interface exceeds the frictional resistance and a stick-slip event occurs over the entire fault plane. Successive events usually cause about the

same amount of average slip (1 cm) between the blocks; but the pattern of slip can vary
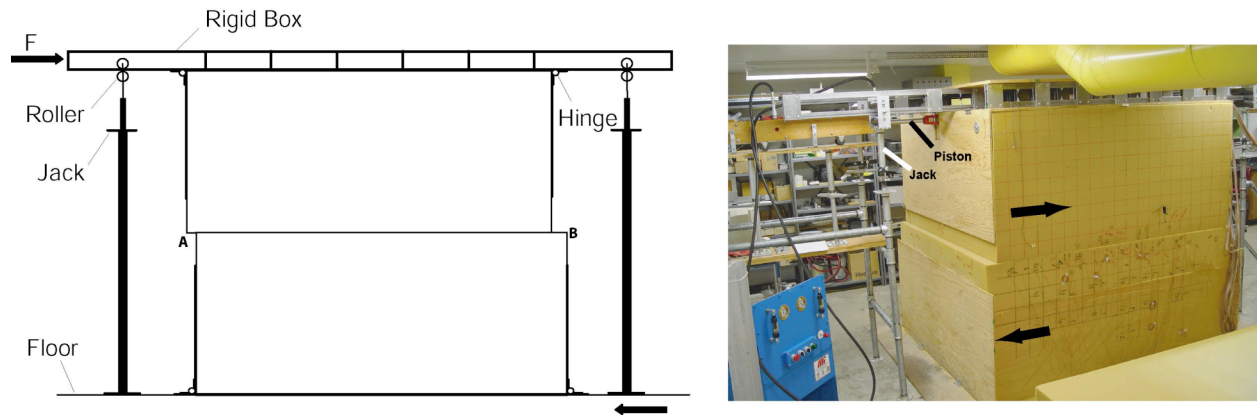
Figure 1: A diagram (left) and a photograph of a foam rubber model of strike-slip faulting.

markedly, with the rupture initiating at different points and propagating in different directions. If the driving displacement is steady, the characteristic events repeat more or less regularly until the upper block has slipped about 20 centimeters, corresponding to about 20 characteristic events with some additional smaller events. At this point, the stress is removed and the upper block lifted and moved back to the starting position for repeat of the procedure. Near the point of shear failure events can be caused to nucleate at different points by slightly raising one or more of the jacks.

MODEL PROPERTIES

Foam rubber is very flexible, that is, it has a low rigidity, making it easy to produce large strains and particle motions. Since foam rubber is lightweight, relatively large models can be constructed, enabling the scale of dynamic phenomena to be enlarged. This allows dynamic features to be more easily observed and recorded using relatively simple electronic devices, such as tiny accelerometers and position sensing devices. The measured properties of the foam rubber used in this experiment are listed in Table 1. Shear wave velocity, β, is slightly anisotropic. The measured velocity perpendicular to the fault is about 36m/s, and parallel to the fault about 38m/s. Appendix B describes the techniques used to measure β. Measuring the compressional wave velocity, α, is less accurate. Our best estimate gives a value around 70 m/s. The rigidity of the model, μ, is calculated from the S-wave velocity and the density.

Table 1: Model Properties

Density	0.016 g/cc
S-Wave Velocity	38 m/s
P-Wave Velocity	70 m/s
Rigidity	2.31×10^5 dyne/cm^2
Q-factor	~10

The coefficient of friction at the contact between the two blocks is greater than unity, and is a function of the normal stress at the contact. Fig. 2 shows plots of pre- and post-event shear stresses as a function of the normal stress.
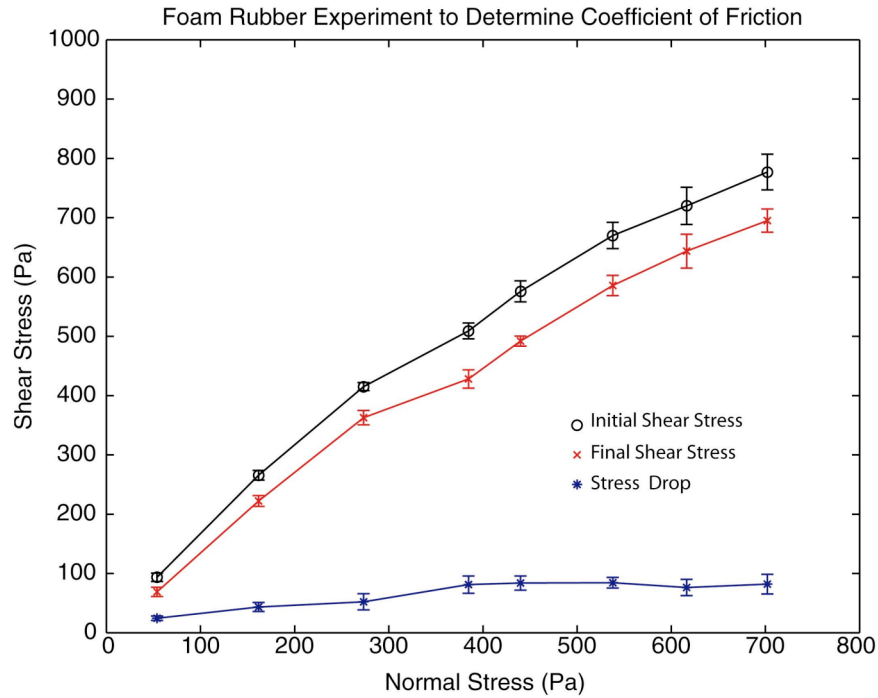
Figure 2: Pre-event and post-event shear stresses are plotted versus the normal stress

Instrumentation

The model is heavily instrumented to record slip-stick events on the fault plane, as well as the free surface. Fig. 3 shows the locations of the sensors. The array consists of 76 recording

3

channels, 35 on the fault plane and 41 on the free surface. The sensors on the fault plane record particle "accelerations" in the y-direction. The sensors on the free surface record fault-normal (z-direction) and fault-parallel (y-direction) particle motions along three profiles parallel to the fault trace at distances of 1, 25, and 45 cm. Sensors numbered 33-60 are "accelerometers", and 65-76 "position detectors". Due to symmetry in the model, all the sensors were placed in the lower block. Appendix A briefly describes the type of sensors and their exact locations in the model.
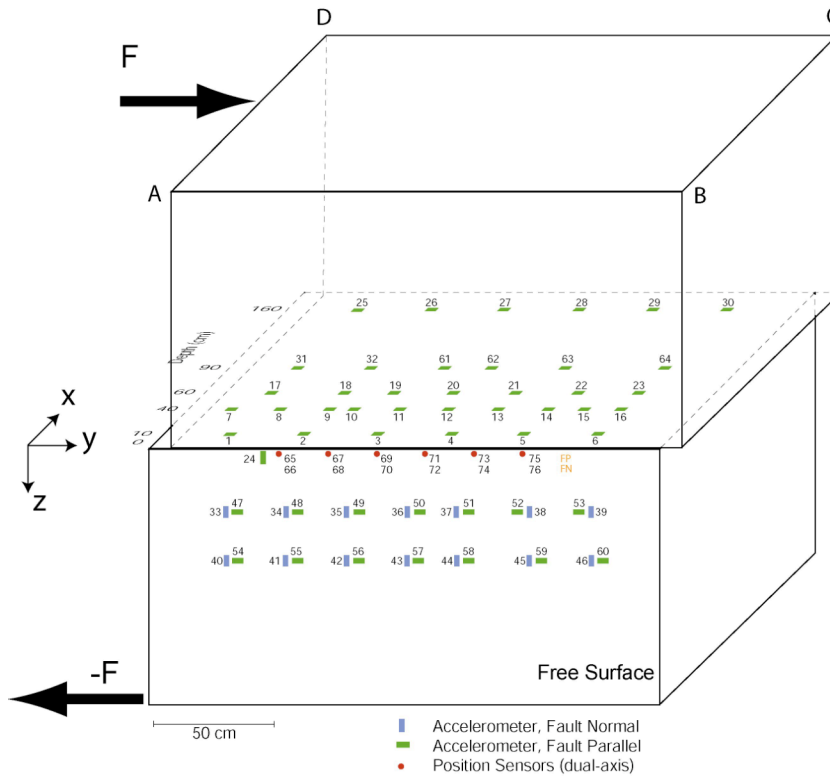
Figure 3: Locations of the sensors in the model.

EXPERIMENTAL RESULTS

Unilateral Rupture

To observe strong directivity, we confine rupture to the shallow part of the fault by (1) stressing the model near the failure point, (2) releasing the stress on the deep section of the fault by raising the scaffolding jacks "C" and "D" (Fig. 3), (3) lowering the lifted side to its initial position, and

4

(4) resuming the stressing of the model until there is a stick-slip event. This procedure ensures several confined stick-slip events to nucleate at one end of the narrow stressed zone and propagate to the other, resulting in a strong forward directivity. Fig. 4 shows the second event after the stress in the deep part of the fault had been released. The normal stress was 538 Pa; the pre-event shear stress about 441 Pa, and the stress drop about 43 Pa. The event is recorded on 76 channels. The numbers next to each trace correspond to the numbers marked on
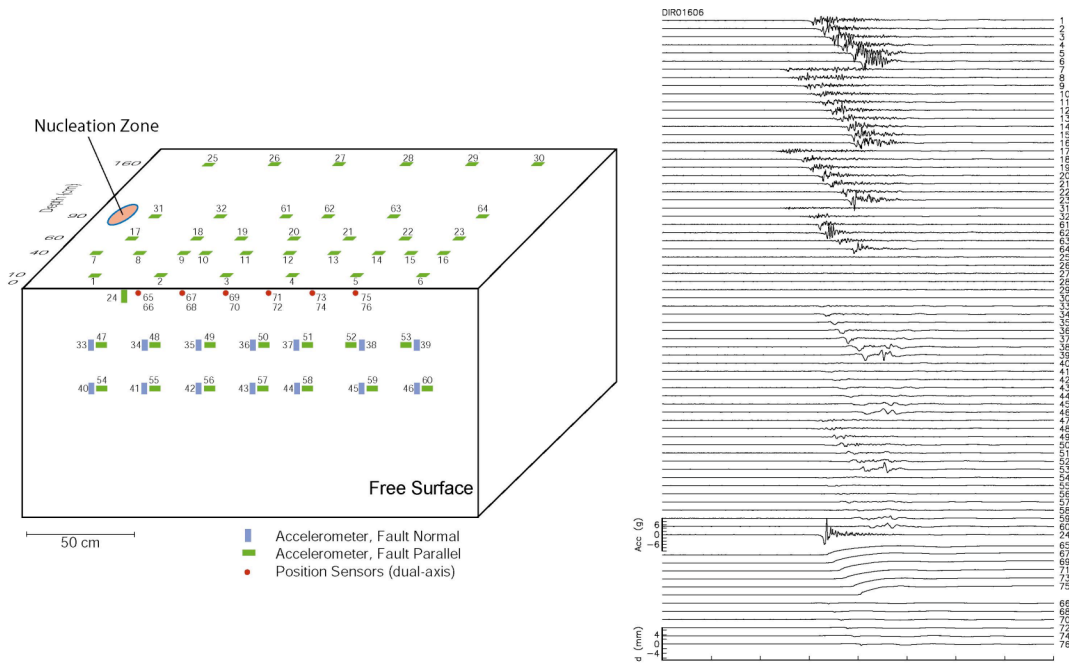
Figure 4: A stick-slip event nucleated near the left edge of the fault propagates to the right, exhibiting strong directivity.

the lower block. The first 64 traces are accelerations, of which 35 are on the fault plane and 29 on the free surface. The last 12 (channels 65-76) are the fault-parallel and fault-normal components of slip at six sites near the fault. The arrival times indicate that the event nucleated at one edge of the fault, near sensors 17 and 31, and propagated unilaterally toward the other edge. Strong directivity is evident from increasing amplitude of the motion at stations further from the nucleation point. As expected, most of the released energy is confined to the shallow part of the fault (stress on the deep part having been released prior to the event). This is obvious from the very low amplitude at sensors 25-30. However, after several events the stress at the deep part builds up again and the amplitude at sensors 25-30 becomes comparable to other sensors on the fault plane. Fig 5 shows one example of this sort. This event nucleated more or less near the

5

nucleation zone of the event shown in Fig. 4. Time series plotted on the left side of Fig. 5 correspond to the accelerations recorded on the free surface along two lines parallel to the fault trace and distances of 25 and 45 cm. Channels 33-46 are the fault-normal components and 47-60 the fault-parallel components. The increasing amplitude at the sites away from the nucleation point demonstrates a strong forward directivity effect. Fig. 6 shows an example of events propagating in the opposite direction of those shown in Figs. 4 and 5.
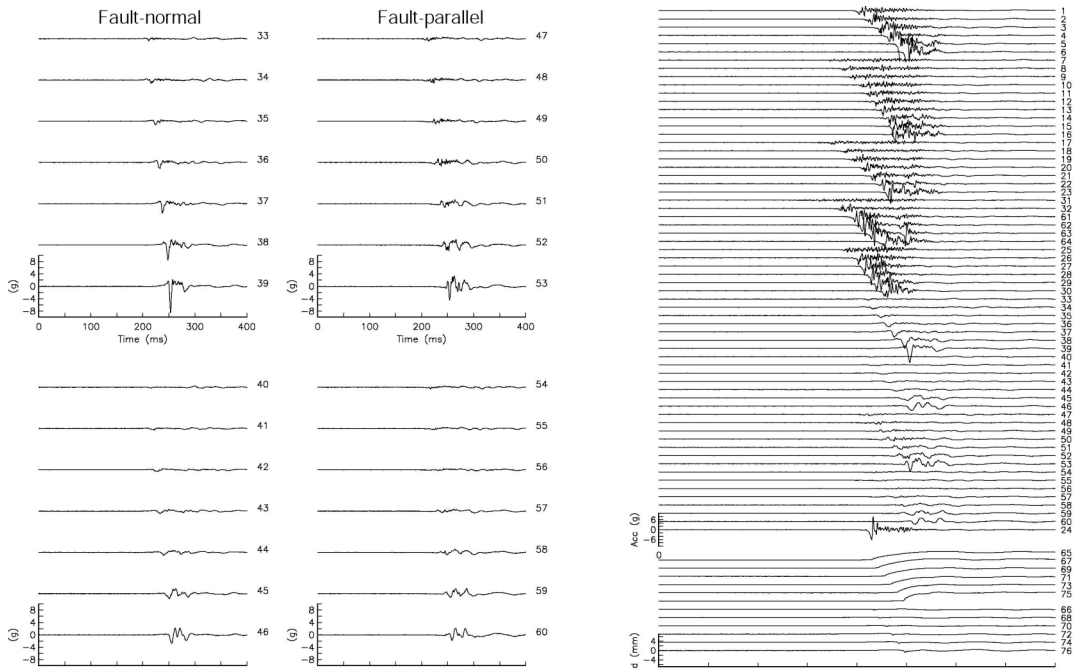
Figure 5: An event rupturing the whole fault after stress on the deep part of the fault had built up again.

Bilateral Rupture

As mentioned earlier, to increase the probability of nucleating events that propagate unilaterally, we reduced the aspect ratio (width/length) of the effective fault plane by releasing the stress on the fault at depth. However, because of a uniform fault plane, under normal conditions the strike-slip events could nucleate at any place on the fault. Fig. 7 shows one event which nucleated near the center of the fault and propagated outward. The rupture arrives at the sensors in the middle of each array first, suggesting a somewhat circular rupture front.
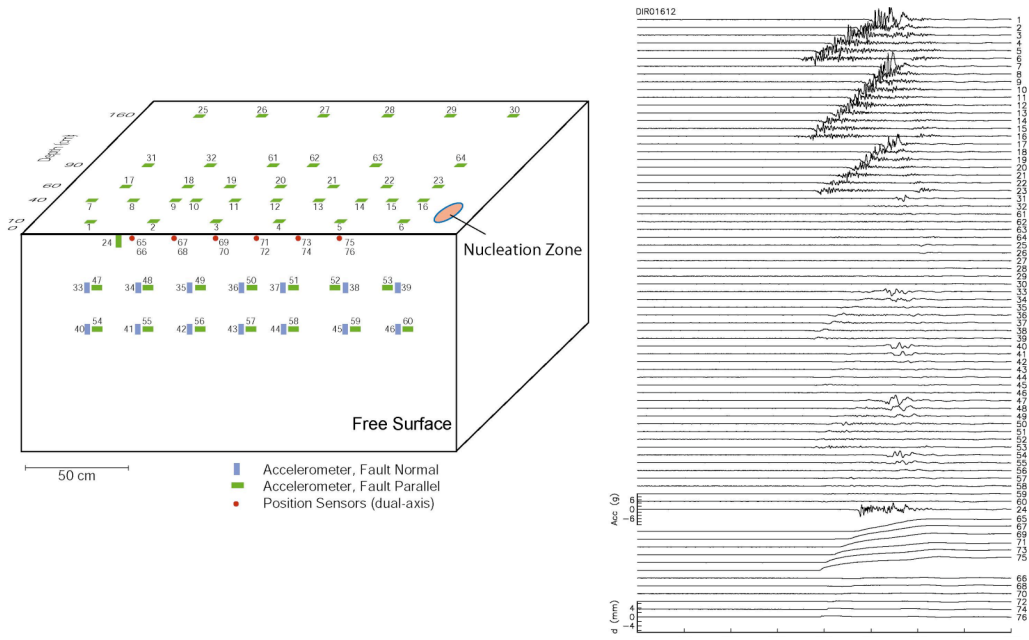
Figure 6: An example of a strike-slip event propagating in opposite direction of those shown in Figs. 4 and 5.
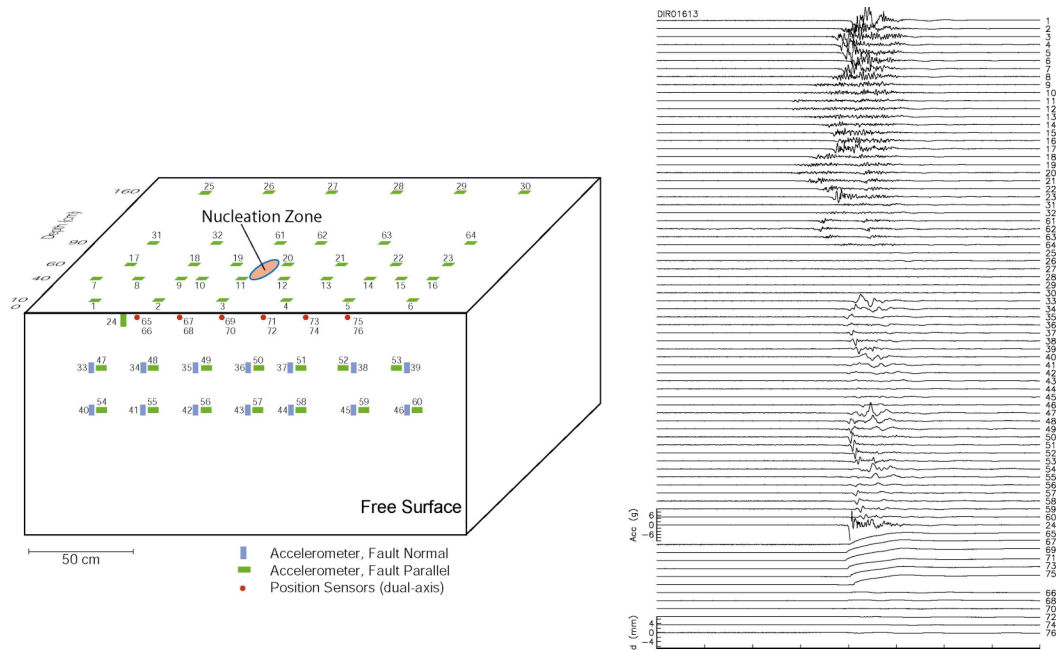
Figure 7: An example of a bilaterally propagating event.

EFFECTS OF ASPERITY ON GROUND MOTIONS

Effects of a Shallow Weak Layer

We also gathered data intended to investigate in detail the effects of a shallow weak layer (model similar to that of Brune and Anooshehpoor, 1998) on the near-fault ground motions. To do this we introduced plastic strips ranging in width from 4 to 20 cm (fault width = 182 cm) on the fault plane. The plastic extends the length of the fault, with one edge at the surface (Fig. 8). An examination of slip accelerations recorded on or close to the weak layer shows significant reduction in amplitudes, even though the total slip is similar to the case without a weak layer (rise time is much longer in the presence of the weak layer). Results of the near-fault surface motions indicate that the acceleration amplitudes decrease rapidly with increasing depth of the weak layer. Fig. 8 shows a recorded event with a weak layer depth of 20 cm, an extreme depth for a weak layer.
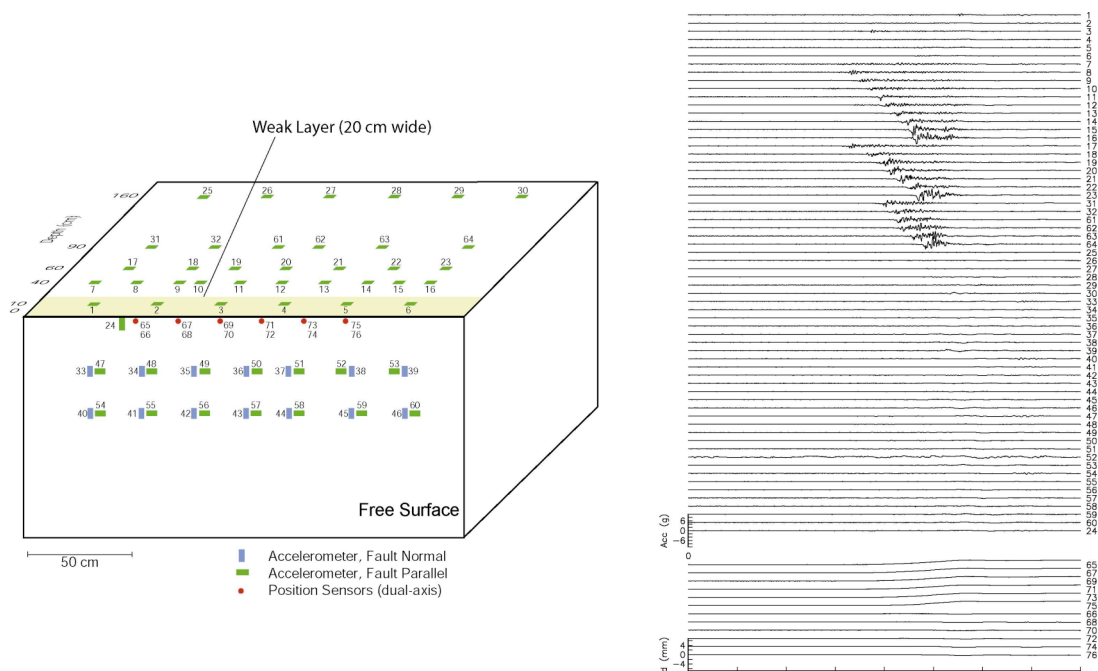
Figure 8: The particle motions for a 20 cm-deep weak layer. The free-surface particle motions (33-60) have all but disappeared.

Effects of a Rigid Anti-Asperity (Weak Patch)

To investigate the effects of an anti-asperity, we placed a thin, smooth circular plate on the fault. The circle is made of fiberglass, and is 25 cm in diameter. One side of the plate is slightly tacky, keeping it in place on the fault. The face in contact with the moving side of the fault (upper block) is smooth. Fig. 9 shows the fault plane and the location of the circular anti-asperity, along with the time histories of a unilateral, shallow rupture showing an effect of asperity. A close
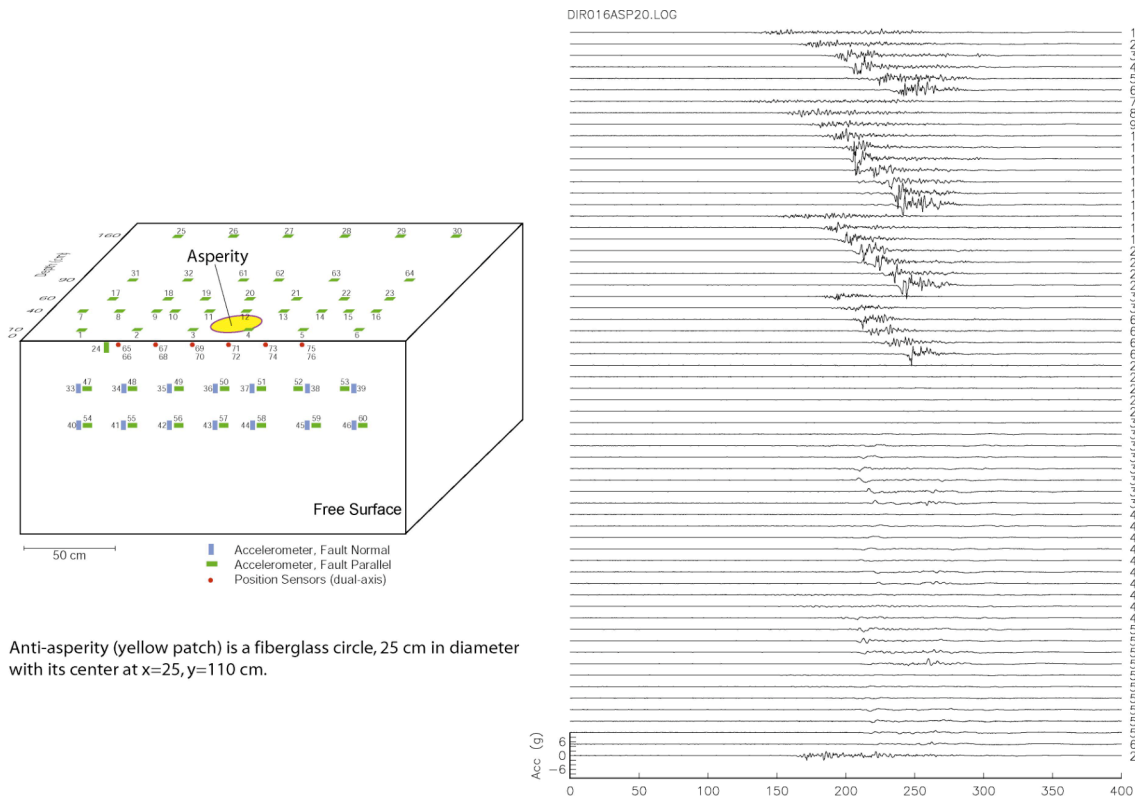
Figure 9: A unilateral shallow rupture showing effects of the anti-asperity.

examination of the fault-normal components of surface motion (chs 33-39) shows a reversal of polarity and opposite move-outs. The reversal takes place near the location of anti-asperity. Fig. 10 shows an event triggered by anti-asperity, with foreshocks. Foreshocks are visible on channels 4, 12 and 13.
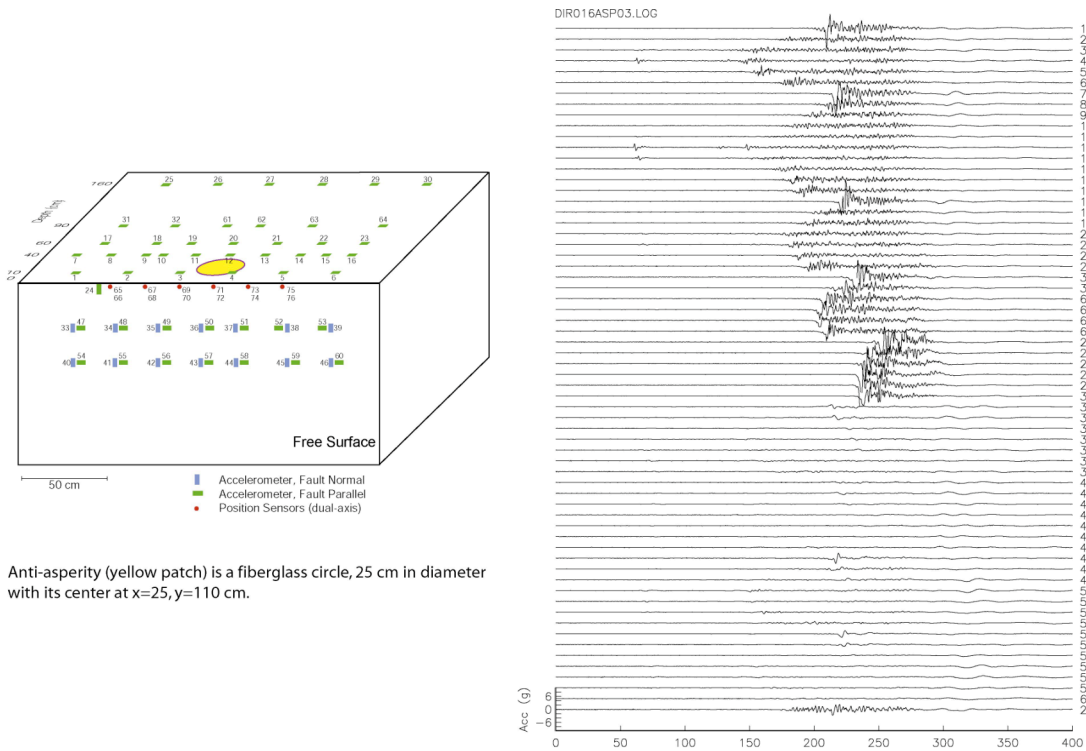
9

Figure 10: The whole block rupture triggered by anti-asperity, with foreshocks.

Effects of Flexible Anti-Asperity

The experiment consisted of a plastic sheet (anti-asperity) approximately 20 cm wide placed on the fault perpendicular to the direction of slip as shown in Fig. 11. The stress was first relieved on the back of the model, causing a mode II rupture (particle motion in the direction of rupture). The rupture propagates from the left of the model to the right. A marked difference in behavior occurred between the responses of channels 69 and 71 in fault parallel displacement; channel 69 has a sharp beginning whereas channel 71 displayed a smooth onset. Unfortunately, channel 73 had noise associated with it (not displayed here), but it appeared to show the same behavior. In comparison, channel 75 shows a shorter rise time and sharp onset. In addition, the static offset recorded over and immediately behind the plastic sheet (with respect to the rupture nucleation site) is somewhat less than the final offset before at channel 75. This may be due to the fact that the action of sliding over the sheet stressed the fault on the other side of the strip without triggering slip there.

10
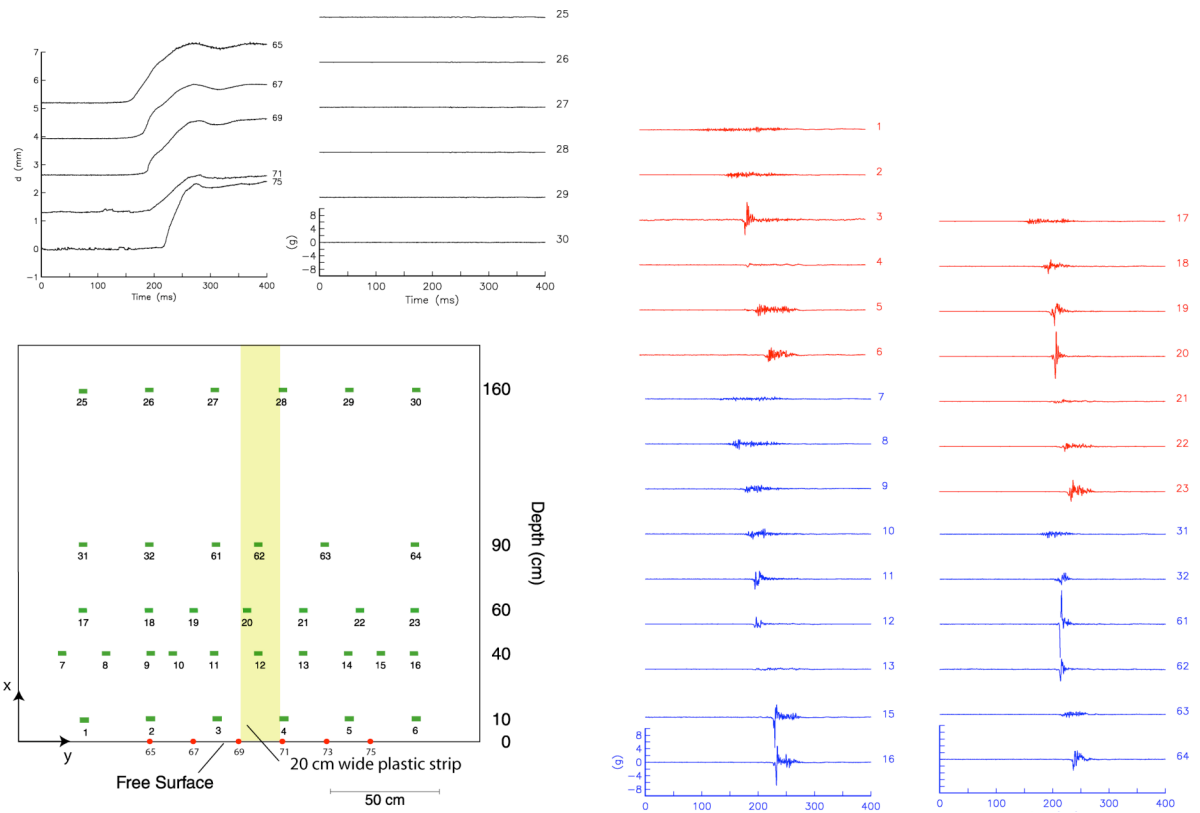
Figure 11: The effects of a soft anti-asperity on ground motions.

The acceleration time histories along the fault in the rupture direction are also intriguing. The rupture did not go through the deep part of the model as seen by the accelerations recorded on the 5th row of accelerometers (channels 25-30). The first row of accelerometers (channels 1-6) shows a nice pulse on the nucleation side of the plastic sheet (channel 3). Right behind the sheet, though, (channel 4) there is very low acceleration. In fact, all instruments right behind the sheet show very little acceleration (channels 4,13,21,63). A few channels some distance behind the sheet, though, show incoherent acceleration time histories reminiscent of nucleation (e.g. channels 5, 6). As one proceeds towards the interior of the model, the peak acceleration amplitudes increase. Note the pulse shape and amplitude of channels 61 and 62. Channel 61 is close to the edge of the plastic sheet on the nucleation side. There is little high frequency energy in the pulse here. The amplitude of channel 62 (over the sheet) is drastically reduced, while the amplitude of channel 63 is very small (right behind the sheet).

These findings suggest that there is a high amplitude fault parallel acceleration pulse near the edge of an anti-asperity (frictional weakness). Over and behind the anti-asperity, the fault

11

parallel accelerations are generally smaller. Some distance behind the anti-asperity, the stress has built to create a sharper onset of displacement and a shorter rise time. There appears to be a stress shadow, though, right after the anti-asperity.

NUMERICAL SIMULATION

Numerical simulations of the stick-slip events in the foam rubber model are performed using the dynamic faulting model of Day (1982). In this three-dimensional finite difference code the rupture growth is spontaneous and governed by a slip-weakening friction law. We used $93 \times 106 \times 96$ nodes with 2 cm spacing. The time step is 0.00015 s. Based on previous simulations by Sarah Gonzalez (Masters Thesis, SDSU, 2003) the slip weakening distance was set at 0.7 mm, static and dynamic coefficients of friction at 1.85 and 1.22, respectively. Boundaries at $z=1$, $z=96$, $y=1$ and $y=106$ are fixed in the code to simulate the presence of plywood sheets in the physical model. Although boundaries at $z=1$ and $z=96$ (top and bottom in Fig. 1) are practically immobile during the rupture, at $y=1$ and $y=106$ they are not immobile at low frequencies. Therefore, in future simulations the code needs to be modified to address this issue.

Figs. 12 and 13 show comparison of an event recorded in the foam-rubber model and its numerical simulation. Fig. 12 compares the free-surface particle motions along the strike of the fault at 1, 25 and 45 cm distances. The accelerations are in units of g and the displacements in mm. Numbers next to each trace correspond to sensors in Fig. 3. Both the fault-normal and fault-parallel components are plotted. At 25 cm and 45 cm distances particle accelerations are plotted, and at 1 cm distance the displacements. Although the accelerations in both models agree well, the displacements do not. Again, a possible source of error could be the choice of fixed boundary conditions at $y=1$ and $y=106$ in the numerical model, which affect low frequencies and consequently the total static offset. Fig. 13 shows comparison of particle velocities on the fault plane in the two models. There is good agreement for low-frequency amplitudes. However the agreement between arrival-times at deeper parts of the fault is poor. As discussed above, this could be due to setting the shear stress on the deeper half of the fault in the numerical model to zero, to simulate the releasing of stress on the fault in the foam-rubber model prior to the event.

12
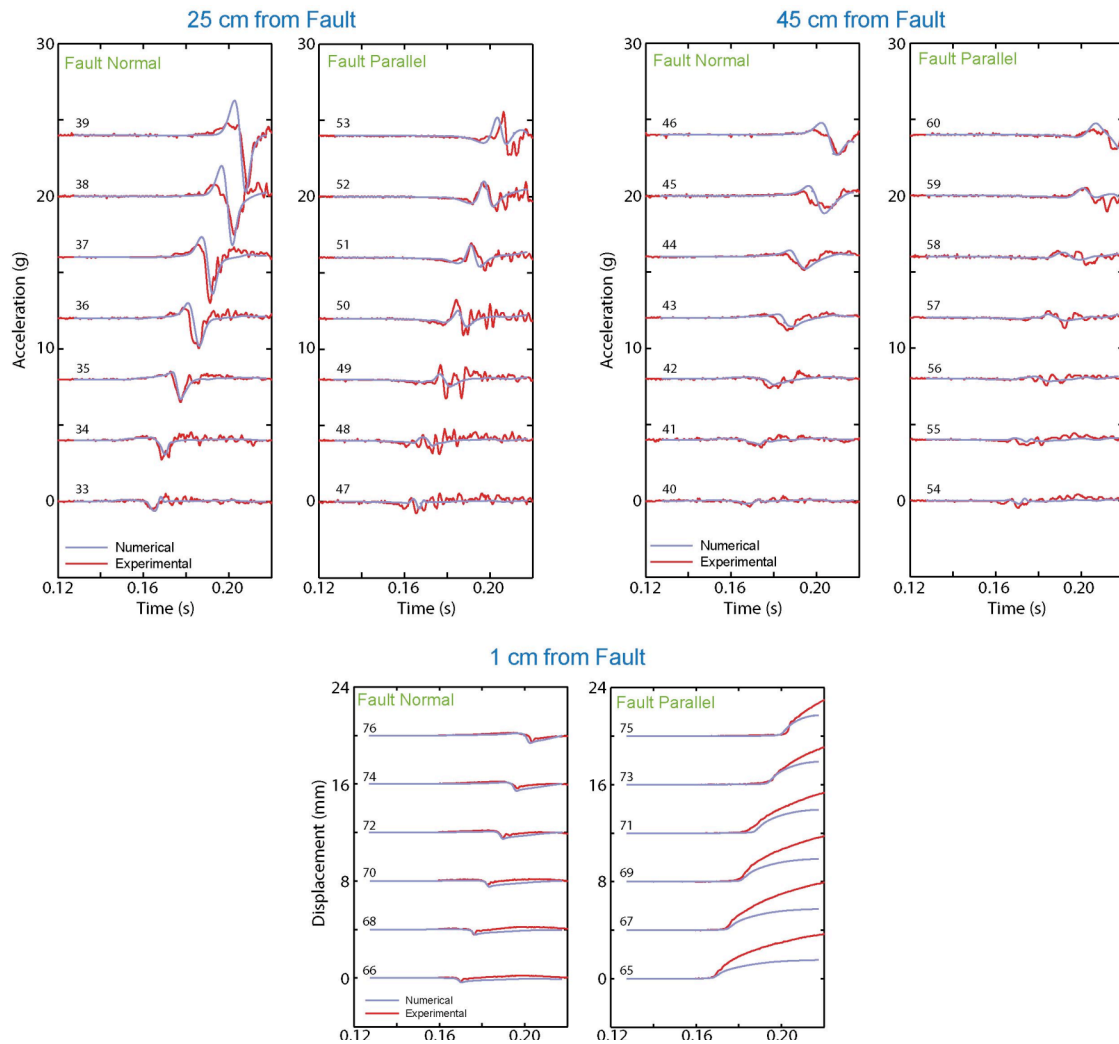
Figure 12: Comparison of free-surface particle motions along the strike of the fault for physical (red) and numerical (blue) models. Both the fault-normal and fault-parallel components are plotted. At 25 cm and 45 cm distances, particle accelerations are plotted and at 1 cm distance the displacement. Although the accelerations in two models agree well, the displacements do not. One possible source of error could be the choice of fixed boundary conditions at y=1 and y= 106 in the numerical model, discussed in the text.

13
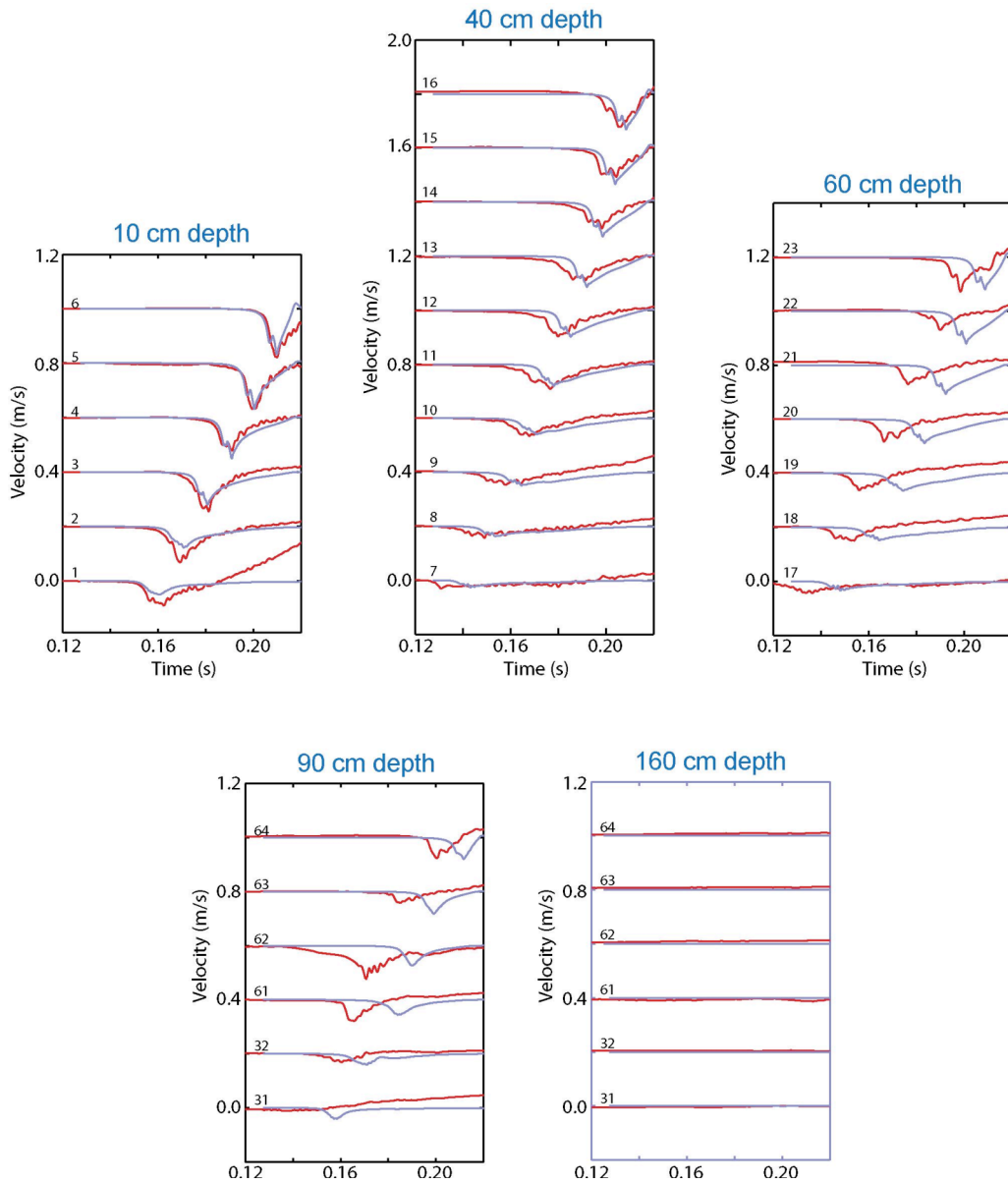
Figure 13: Comparison of particle velocities on the fault plane for physical (red) and numerical (blue) models. There is good agreement in the low-frequency amplitudes in both models. However the agreement between arrival-times at deeper parts of the fault is poor. This could be due to setting the shear stress on the deeper half of the fault in the numerical model to zero, to simulate the releasing of stress on the fault in the foam-rubber model prior to the event. However, in reality the stress at the depth in the physical model is low but non-zero. This could slow down the rupture velocity in numerical model more than the physical model.

14

Gonzalez (2003) investigated the effect of directivity on horizontal spectral acceleration. Residuals were computed by removing the mean effect of distance (measured to the nearest point on the fault) from each horizontal-component spectral value. For each event, the mean of the natural logarithm of both fault-normal and fault-parallel spectral components at a distance of 25 cm from the fault was obtained. This value was then subtracted from the natural logarithm of each individual spectral value to obtain the residuals. This process was repeated for the horizontal-component spectral values at a distance of 45 cm from the fault.

Residuals for both the foam events and numerical simulation were plotted as a function of the directivity variable $X\cos(\theta)$ (Fig. 14). Regressions for the residuals as a function of $X\cos(\theta)$ are shown in Fig. 15 for both the numerical model (NM, black lines) and the physical model (PM, red lines). Each subplot shows regression lines for one period. A comparison of the numerical and experimental regression results with those for empirical earthquake model of Somerville et al. (1997), indicate good agreement at long periods. However, the physical and
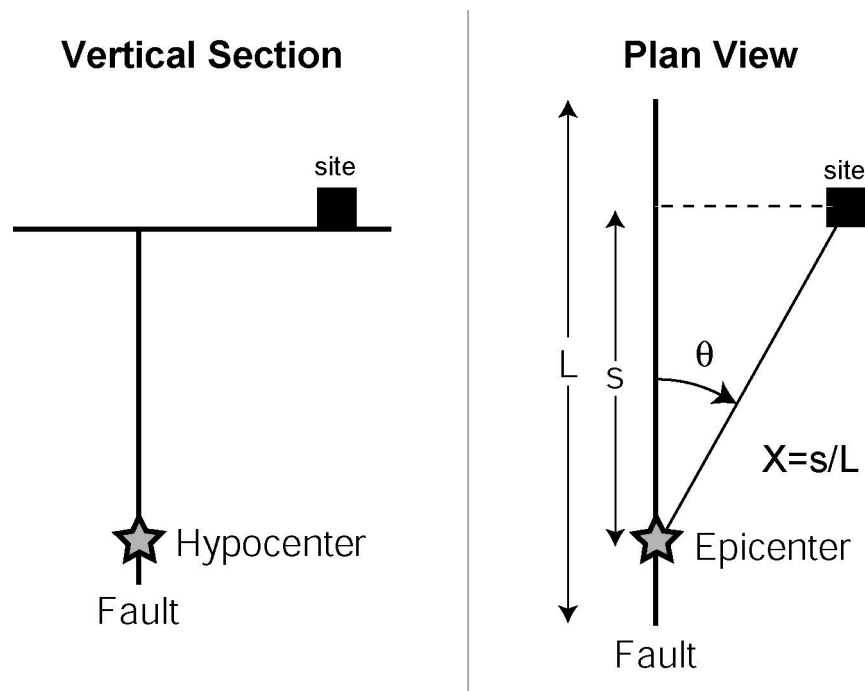
Figure 14: Schematic showing rupture directivity parameters θ and X (after Somerville et al., 1997).

numerical models consistently over-predict the empirical model at shorter periods, with over-prediction increasing systematically as the period shortens. This is probably an effect of the incoherency in high frequencies in the physical model, which is not incorporated in the numerical model.
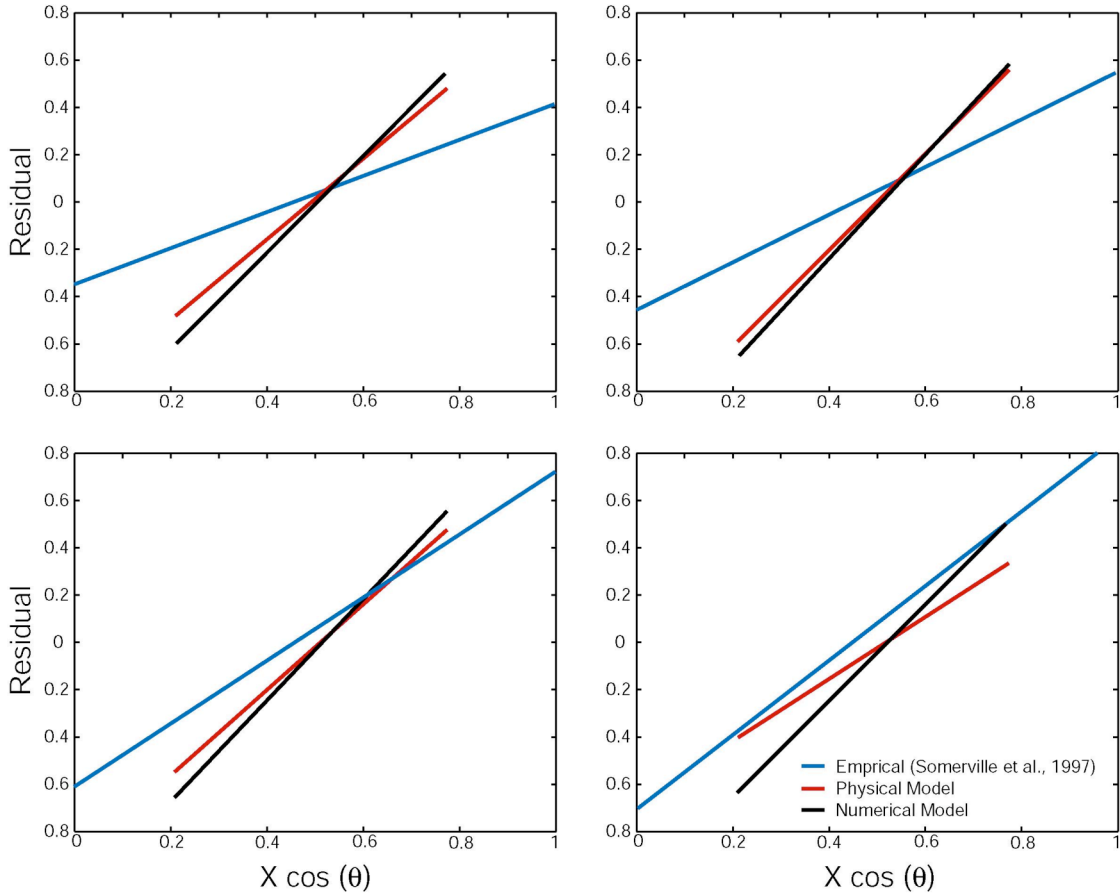
Figure 15: Regression lines for the residuals as a function of the directivity variable $X\cos(\theta)$**, for the numerical model (NM), physical model (PM), and the empirical model of Somerville et al., 1997.**

CONCLUSIONS

Data from foam-rubber earthquake experiments simulating unilateral strike-slip rupture indicate strong directivity effects. The data agreed well with 3D numerical simulations of the shape, duration, and absolute amplitude of the direct acceleration pulses. Directivity was evident in both peak accelerations and pseudo-spectral accelerations, the amplitude of the fault-normal component of acceleration generally larger than the associated fault-parallel component. Waveforms agree with an empirical directivity model for earthquake strong-motion spectra at long periods.

The presence of a weak layer (plastic strips of different widths) on the shallow part of the fault has a strong effect on ground motions. Accelerations recorded on or close to the weak layer show significant reduction in amplitudes, even though the total slip is similar to the case without a weak layer (increased slip rise-time). Results indicate a rapid decrease in the amplitude of surface accelerations with increasing depth of the weak layer.

Based on these results, we believe foam-rubber modeling has the potential for better understanding of the rupture process and ground motion effects in the near field, and validation of simulation methods which can be applied to a wide variety of cases and eventually provide realistic forward simulations for time-history based design.

REFERENCES

Brune, J. N., S. Brown, and P. A. Johnson. 1993. Rupture mechanism and interface separation in foam rubber models of earthquakes: a possible solution to the heat flow paradox and the paradox of large overthrusts. *Tectanophysics* 219: 59-67.

Brune, J.N., A. Anooshehpoor. 1998. A physical model of the effect of a shallow weak layer on strong ground motion for strike-slip ruptures. *Bull. Seism. Soc. of Am.* 88, 1070-1078.

Day, S. M. 1982. Three-dimensional finite-difference simulation of fault dynamics: rectangular faults with fixed rupture velocity. *Bull. Seism. Soc. of Am.* 72, 705-727.

Gonzalez, S. H. 2003. Foam rubber and numerical simulations of near-fault seismic directivity. 2003. Master's Thesis, San Diego State University.

Somerville, P. G., N. F. Smith, R. W. Graves, and N. A. Abrahamson. 1997. Modification of empirical strong ground motion attenuation relations to include the amplitude and duration effects of rupture directivity. *Seism. Res. Lett.* 68(1), 199-222.

APPENDIX A

Position-Sensing Detectors

Displacement at the foam surface is measured by a telescopic, 2-axis, position-sensing detector, which is focused on a small light emitting diode (LED) embedded in the foam. The Dual Axis Super Linear Position Sensor (DLS10, manufactured by the United Detector Technology Sensors, Inc.), is a square of photovoltaic material, 1 cm on a side. The sensor locates the centroid of a light spot (image of the embedded LED) projected upon it, and provides continuous output as the light spot moves from the null point to either direction along each of the two perpendicular axes. The output of the position-sensing detector depends on the location as well as the intensity of the bright spot. Therefore, it is necessary to calibrate detectors before and after each experimental run (The position detectors have a built-in calibrating mechanism.). The resolution of the DLS10 sensors is limited only by the intensity of the light source and the signal resolving circuitry. In our experiments, the resolution is better than 0.01~cm.

Ultra-light Accelerometers

Due to foam rubber's low density and high elasticity, particle accelerations in a stressed foam rubber model of earthquakes can exceed several hundred g (the acceleration due to gravity). Slips of the order of 1 cm can take place in a few milliseconds, resulting in very large accelerations at high frequencies. In order to measure these accelerations, accelerometers with a high dynamic range and low mass (to minimize the mass loading effects) are needed. We use ultra-light ENDEVCO Model 25A accelerometers (Fig. A-1). The Model 25A, has a mass of 0.2 gm, a dynamic range of 1000 g, and a flat response from about 1 hz to about 20 khz. In order to further reduce the mass loading effects, each accelerometer is mounted on a styrofoam disk, 3.8 cm in diameter, before inserting them in the foam; the 3 mm thick styrofoam disk (with the same density as the foam rubber used in the model, but far more rigid) distributes the accelerometer's mass over a larger area (about 50 times larger).
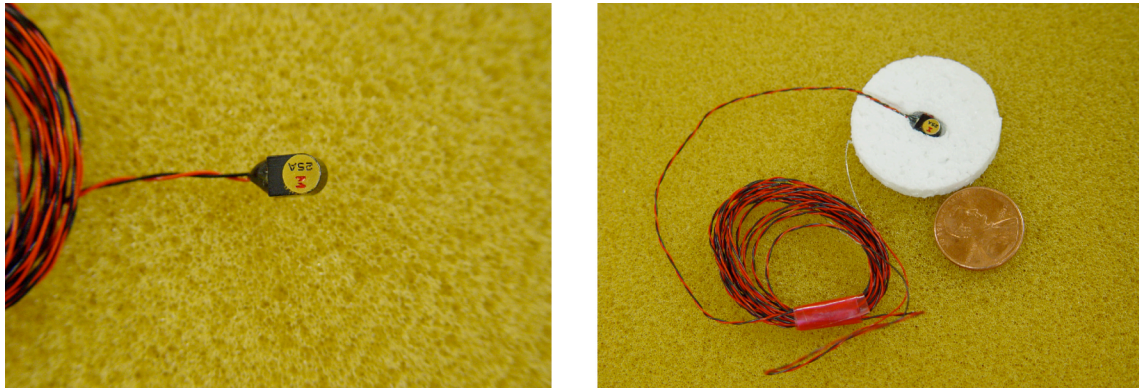
Figure A-1: Photographs of the ENDEVCO 25A accelerometer before and after it was mounted on a thin Styrofoam disk to reduce the mass-loading effect.

Sensor Locations

Tables A-1 and A-2 list the coordinates and orientation of each sensor (see Fig. 3). Table A-1 lists the location of position sensors in the model and Table A-2 the accelerometers.

Table A-1: Coordinates and Orientation of Position Sensors

| Channel Number	Coordinates			Sensor Orientation
	X (cm)	Y (cm)	Z (cm)	
65	61	0	-1	FP
66	61	0	-1	FN
67	81	0	-1	FP
68	81	0	-1	FN
69	101	0	-1	FP
70	101	0	-1	FN
71	121	0	-1	FP
72	121	0	-1	FN
73	141	0	-1	FP
74	141	0	-1	FN
75	161	0	-1	FP
76	161	0	-1	FN

Table A-2: Coordinates and Orientation of Accelerometers

| Channel Number	Coordinates			Accelerometer S/N	Sensitivity (Counts/g)	Sensor Orientation
	X (cm)	Y (cm)	Z (cm)			
1	29	10	-3	BK49	165.70	FP
2	60	10	-3	CT89	162.10	FP
3	90	10	-3	AC77	144.71	FP
4	121	10	-3	AC68	144.54	FP
5	151	10	-3	AC46	141.05	FP
6	182	10	-3	AC36	136.63	FP
7	20	41	-3	CT01	145.33	FP
8	40	41	-3	AB09	145.72	FP
9	60	41	-3	CT03	145.20	FP
10	71	41	-3	AC11	143.07	FP
11	89	41	-3	CT25	172.63	FP
12	109	41	-3	BK46	160.86	FP
13	129	41	-3	CT54	174.56	FP
14	150	41	-3	AB20	149.74	FP
15	165	41	-3	CK29	153.63	FP
16	180	41	-3	BK52	147.45	FP
17	29	60	-3	CW54	149.68	FP
18	59	60	-3	CW62	145.95	FP
19	79	60	-3	CW58	150.76	FP
20	104	60	-3	CW76	145.86	FP
21	129	60	-3	CW86	143.92	FP
22	155	60	-3	CW64	151.54	FP
23	180	60	-3	CW68	154.88	FP
24	56	3	-4	BK44	156.94	FP
25	29	160	-3	CW34	144.58	FP
26	59	160	-3	CW36	152.36	FP
27	89	160	-3	CW37	160.83	FP
28	120	160	-3	CW42	153.50	FP
29	150	160	-3	CW43	149.71	FP
30	180	160	-3	CW45	154.19	FP
31	29	90	-3	CW47	161.06	FP
32	59	90	-3	CW48	154.09	FP
33	35	3	-25	CR92	139.08	FN
34	55	3	-25	BK40	163.15	FN
35	80	3	-25	CT90	167.50	FN
36	105	3	-25	AB18	146.28	FN
37	125	3	-25	CT93	191.00	FN
38	155	3	-25	BK38	153.24	FN
39	175	3	-25	CW70	140.33	FN
40	35	3	-45	CW79	161.15	FN
41	55	3	-45	CT84	172.53	FN
42	80	3	-45	CT72	165.24	FN
43	105	3	-45	CT67	169.36	FN
44	125	3	-45	AC45	147.13	FN
45	155	3	-45	CW03	164.26	FN
46	175	3	-45	CK24	143.53	FN
47	40	3	-25	CR91	133.95	FP
48	60	3	-25	BK41	158.57	FP
49	85	3	-25	CT91	159.36	FP
50	110	3	-25	AB39	145.49	FP
51	130	3	-25	CT94	173.84	FP
52	150	3	-25	AB50	144.22	FP
53	170	3	-25	CW71	150.33	FP
54	40	3	-45	CR87	144.35	FP
55	60	3	-45	CT86	164.95	FP
56	85	3	-45	CT78	144.94	FP
57	110	3	-45	CT95	174.69	FP
58	130	3	-45	CW05	141.31	FP
59	160	3	-45	CW07	159.91	FP
60	180	3	-45	CN37	166.42	FP
61	89	90	-3	CW49	121.79	FP
62	109	90	-3	AC66	144.54	FP
63	139	90	-3	CW50	163.34	FP
64	180	90	-3	CW51	150.30	FP

Shear-Wave Velocity Measurements

Shear-wave velocity is calculated by measuring the travel time between an impulsive shear source and a receiver. The shear source is a square fiberglass plate glued to the foam. An impulsive electromotive driver moves the plate in a plane perpendicular to the line between the source and receiver. An electric pulse, generated by the digital recorder, triggers a shear pulse. Both the trigger pulse and the shear wave at the receiver site are recorded. The travel time is measured from the time difference between the onset of the trigger pulse and the first shear-wave arrival at the receiver. Fig. A-2 shows the setup to measure shear-wave velocity along a line perpendicular to the fault plane (Fig. 3). This measurement was done several years ago, before the construction of the model. The measured shear-wave velocity was about 36 m/s.
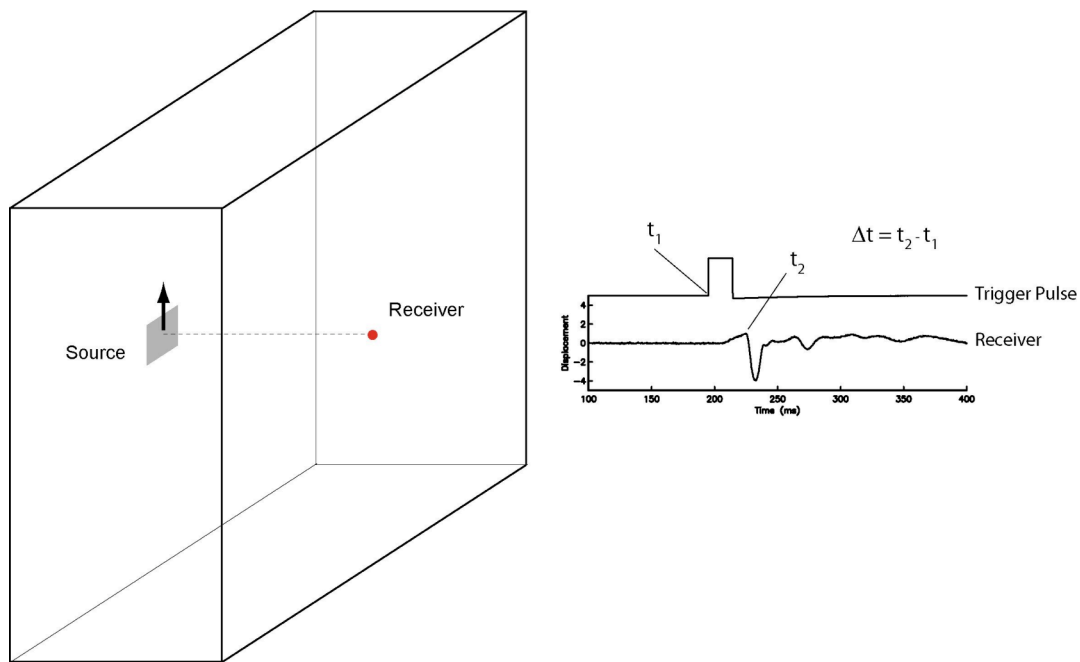
Figure A-2: Setup for measuring shear-wave velocity perpendicular to the fault plane.

For this project we decided to measure the shear-wave velocity again. However, it was impossible to repeat the above measurement without dismantling the model. Instead, we decided to use the setups shown in Fig. A-3. The measured shear-wave velocity was 38.00±0.33 m/s,

and 38.54±0.14 m/s, for setups (a) and (b), respectively. This discrepancy between velocities parallel and perpendicular to the fault is attributed to the anisotropy of foam rubber.

(a)

(b)
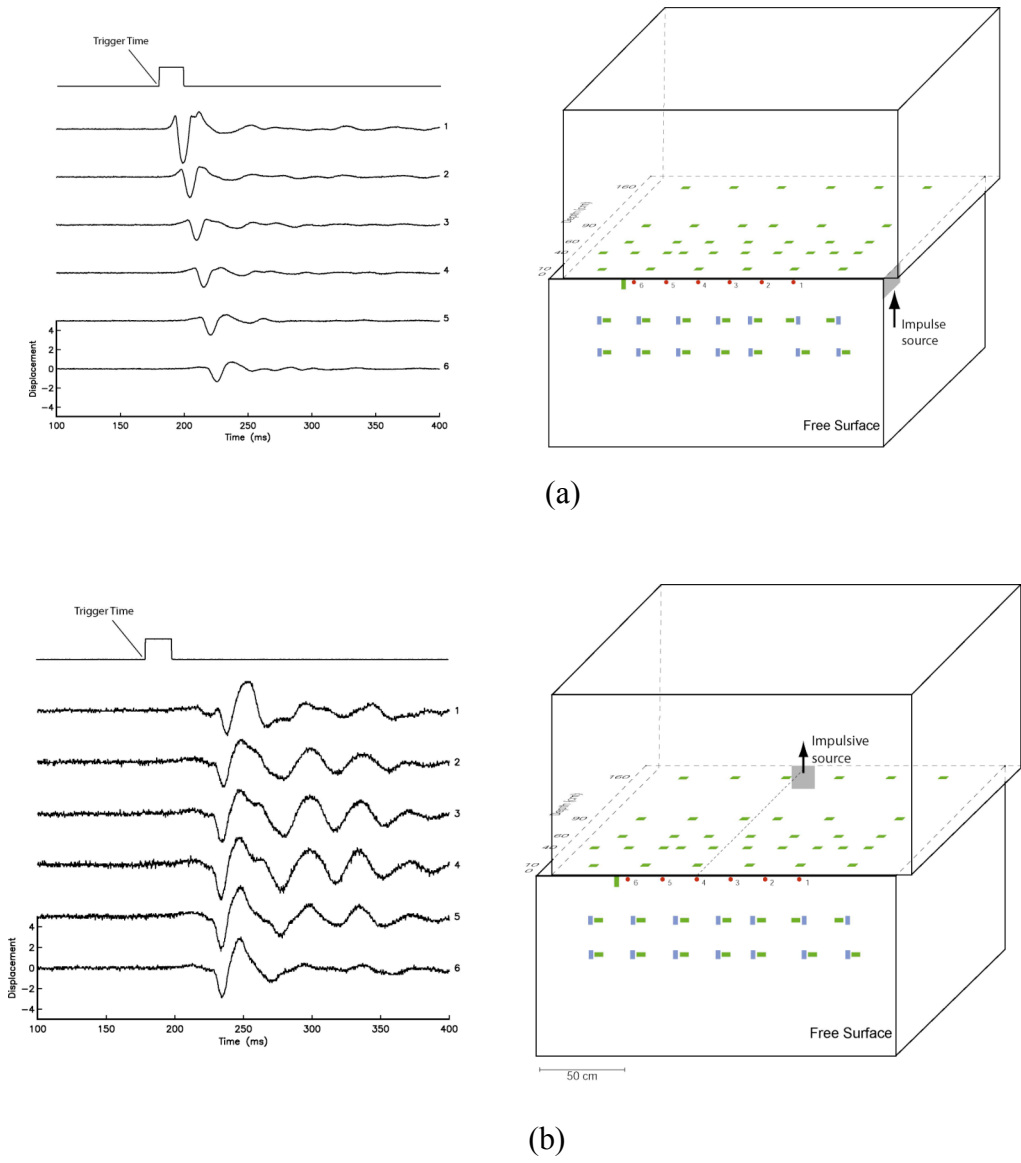
Figure A-3: Setups and waveforms recorded at stations 1 through 6, along the fault trace are shown here. The travel times between the source and receiver were used to calculate the shear-wave velocity in the model, parallel to the fault plane.